33RD CONGRESS
OF THE INTERNATIONAL COUNCIL
OF THE AERONAUTICAL SCIENCES
STOCKHOLM, SWEDEN, 4-9 SEPTEMBER, 2022

ICAS 2022 SWEDEN

WIND-TUNNEL TEST ON LEADING-EDGE VORTEX OF LOW-ASPECT-RATIO FLAPPING PLATES

Jong-Seob Han & Christian Breitsamter

Chair of Aerodynamics and Fluid Mechanics, School of Engineering and Design,
Technical University of Munich, Germany

Abstract

A leading-edge vortex attaching to the suction side of a wing was one unique phenomenon explaining a high lift force of sweptback aerodynamic devices as well as the wings of biological flyers. In forward flight, however, various parameters and their relationships at low Reynolds number complicate the study. Here, we prepared a servo-driven robotic arm, force/torque transducers for six axes, and several model plates with different aspect ratios for the wind tunnel test. A way of eliminating an inertial force and decomposing steady and unsteady components were also discussed. In a preliminary test, we found that a sweptback angle provided a better lift for all the plates regardless of aspect ratio. The plate with an aspect ratio of three outperformed the others with a sufficient sweptback angle, as a previous study found. A further test for the plates in sweeping motion showed an increase in the lift with time at a non-zero sweptback angle during the stroke; this is also in line with a previous study. The test with two different thickness plates clarified the potential of the approach of how to remove inertial forces from the measured values in motion.

Keywords: Wind-tunnel test, Leading-edge vortex, Flapping/revolving wing,

1. Introduction

A leading-edge vortex (LEV) attaching to a suction side of a wing is one unusual flow structure responsible for a high lift force. This has been found on delta wings and sweptback wings where the LEV forms with a spanwise flow [1], as well as on the wings of biological flyers where the wingbeat motion produces the pressure gradient along a wingspan [2]. These LEVs do not only provide a lower pressure on the suction side of the wings by themselves, but also stabilize the flow over the wing with higher inertia thereby satisfying the Kutta condition at the trailing edge where unstable shed vortices usually appear.

As the biofluiddynamically scaled Navier-Stokes equation points out [3-4], the LEV of flapping wings is governed by an aspect ratio AR and an advance ratio J. For AR, Han et al. [5] investigated aerodynamic characteristics of flapping wings with several different ARs during hovering, and showed that the AR = 3.0 results in the highest lift force with a reasonable efficiency at a Reynolds number of ~10^4. They further pointed out that this might be a reason why some species of insects such as hawkmoths, hoverflies, bumblebees, and fruit flies, which are all adept at hovering, have the AR near three. Kruyt et al. [6] investigated a LEV structure with respect to AR, and found that the LEV can only be sustained around four times the chord from the wingroot. Jardin and Colonius [7] simulated flow structures around revolving wings with several different AR. They showed an inboard stable LEV growth, which only reaches three times the chord as a limit. After this limit, the outboard unstable shedding appeared. They also agreed that the wing with AR = 3.0 produces the highest lift at least within the geometry of the wings of biological flyers, i.e., a wingroot-fixed revolving/flapping motion.

Compared to the AR, LEVs in forward flight have not been sufficiently studied. This seems to be due to additional parameters and relationships that should be considered with freestream and forward flight, as Han and Breitsamter [8] pointed out.

A stroke plane angle, which is usually inclined and shifted back with an increase in flight speed, is one major parameter in forward flight. A consequent change in instantaneous angles of attack, which would be distributed along the wingspan, is another crucial parameter determining LEV behaviors and overall aerodynamic characteristics. The J is a coefficient of the two acceleration terms in the Navier-Stokes equation as the AR is, implying that it is also one dominant parameter determining LEV characteristics.

In order to unravel the effect of freestream and wingbeat kinematics on the LEV in forward flight, we prepared a servo-driven robotic arm, a six-axis force/torque transducer, and several model plates with different ARs. The robotic arm can be simultaneously driven by an in-house control code that was synchronized with the measurement DAQ system, and the transducer was designed exclusively for this study. The plates were designed considering both the rigidity and the lightweight for the lowest inertia during the motion.

2. Experimental Setup and Procedure

2.1 Three-Rotational Axes Robotic Arm

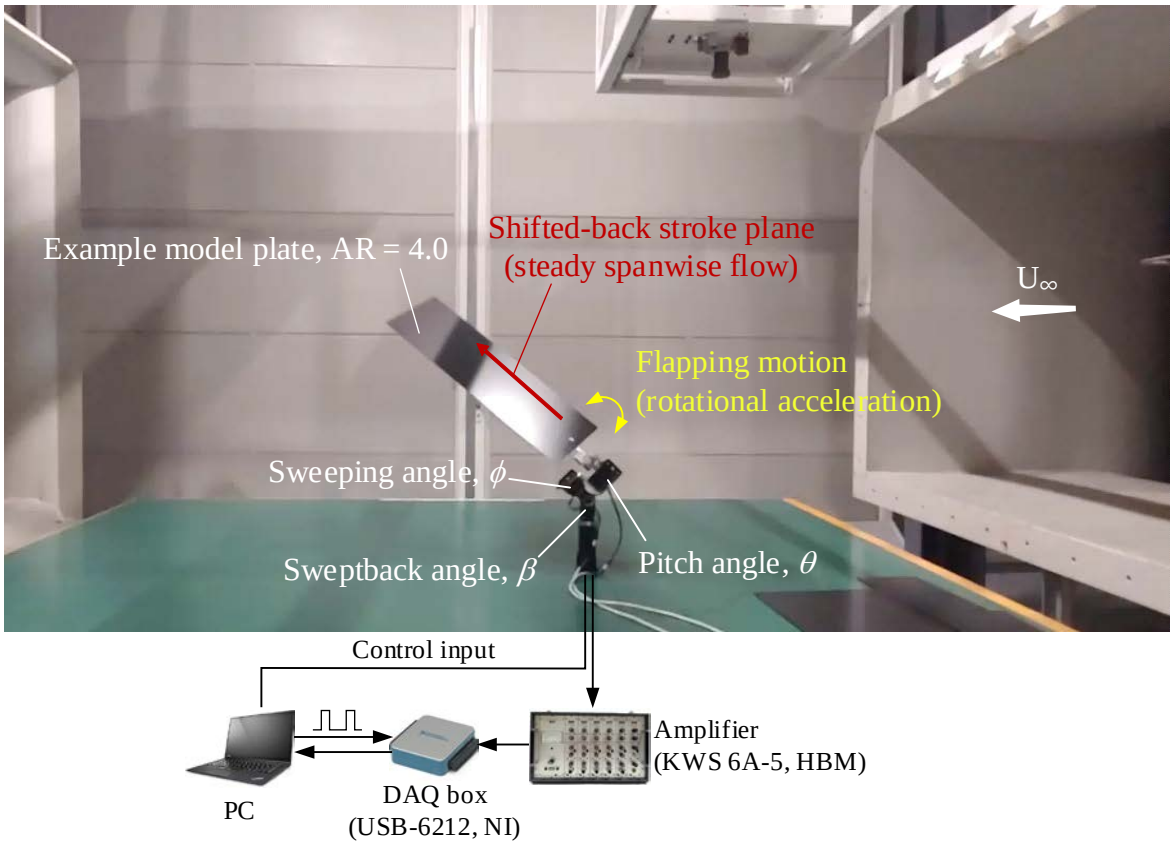

Figure 1 – Three-rotational-axis robotic arm on the test section of wind tunnel B

Figure 1 shows the three-rotational axes robotic arm mounted on the test section of wind tunnel B at the Technical University of Munich (refer to [10] for more detail about the wind tunnel). The encoders equipped in the servo motors (MX540, Robotis®) have a resolution of 4096 steps/rev (0.088 deg/step). The baud rate of 4.5 Mbps of each motor allows precise control and tracking in the angular positions. The motors also have sufficient torque at a designated wingbeat amplitude and frequency (±45 deg at 1 Hz). Each motor directly controls the rotating axes of the sweptback angle β, sweeping angle ϕ, and pitching angle θ. Due to the structural constraint, however, β, ϕ, and θ only have the range of 0 to 90 deg, ±60 deg, and ±90 deg, respectively. The corresponding freestream at J = 1.0 can be up to ~2.7 m/s.

2.2 6-axis Force/Torque Transducer

The motion of the model plates would only create a dynamic pressure under a few pascals, meaning

that it would rarely be possible to collect the force/torque by a commercial transducer. To this end, we designed a single axis force/torque bending beam loadcell, and constructed them for the three axes, as shown in Figure 2. Each loadcell consists of two pairs of straingauges (1-LY93-3/350E, HBM), which were mounted on the beam in a row, thereby giving two bending moments at two different positions across two individual channels. The normal force can be then obtained by the two torques and a distance between the locations of each set of straingauges (refer to Fig. 2 and Han et al. [5] for details). We installed these three loadcells at the end effector of the arm for each axis. A total of six channels were used to collect the data. Here, the correlated force component to the other axis which can give the same moment is also canceled by a structural constraint.

Figure 3 shows a calibration curve of the one bending beam loadcell. Each moment on the set of straingauges was directly proportional to the voltage. Here we also used the gap between the two y-intercepts as a way of finding the distance *d*.

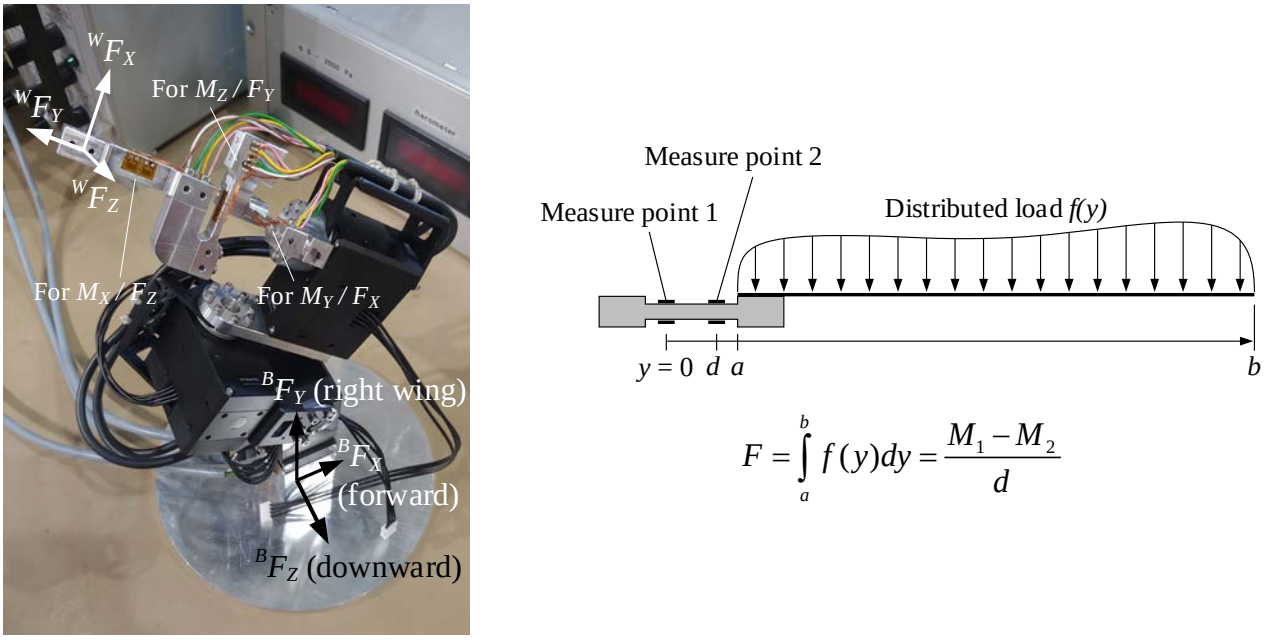

Figure 2 – Bending-beam type 6-axis force/torque transducer

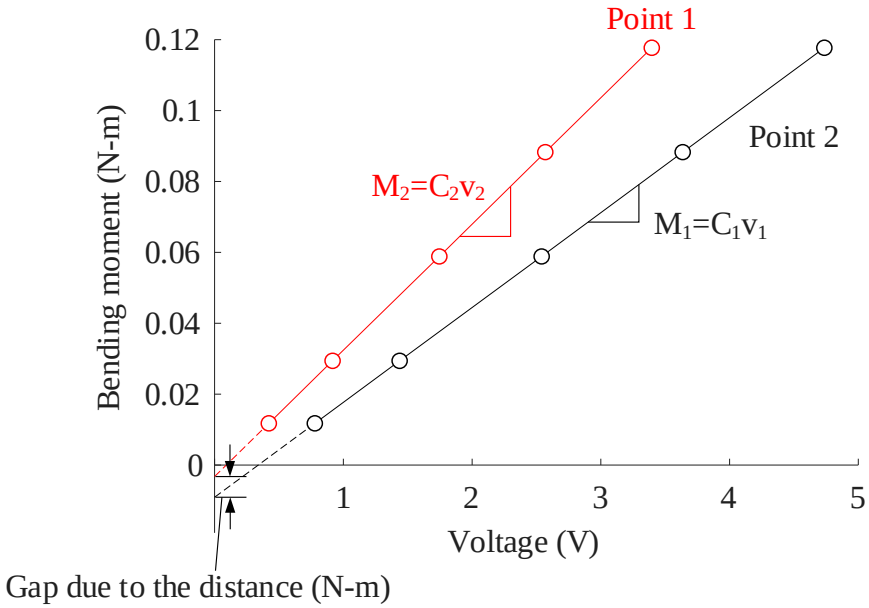

Figure 3 – Calibration curves of the loadcell for M_X and F_Z.

2.3 Low-AR Plates and Deformation in Motion

A wingbeat motion of the plates always produces structural deformation. Most of the deformation appears along the wingspan, affecting chordwise sectional stroke velocity, which eventually changes an inflow direction, velocity, and a consequent angle of attack as shown in Eqs. (2) and (3). Thus, evaluating and reducing the effect as much as possible is a prerequisite for accurate measurement.

$$U_{\text{inflow}} = \sqrt{U_{\infty}^2 + (\dot{\phi} r)^2} \tag{2}$$

$$\alpha = \theta + \tan^{-1} \frac{\dot{\phi} r}{U_{\infty}} \tag{3}$$

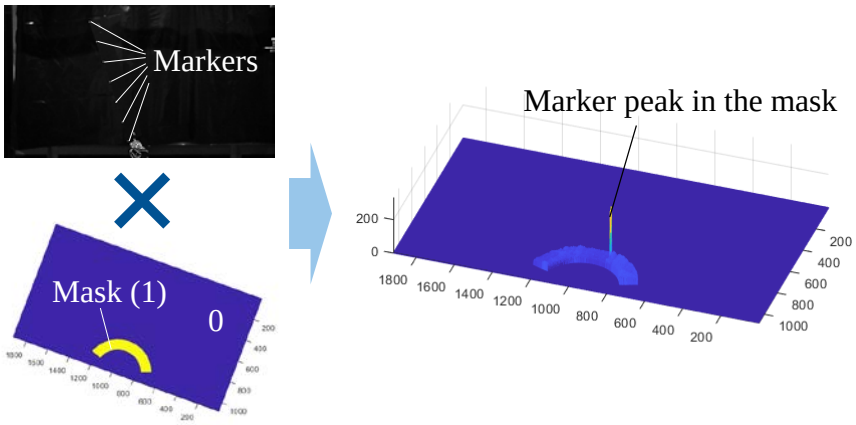

Figure 4 – Post-processing for the deformation extraction

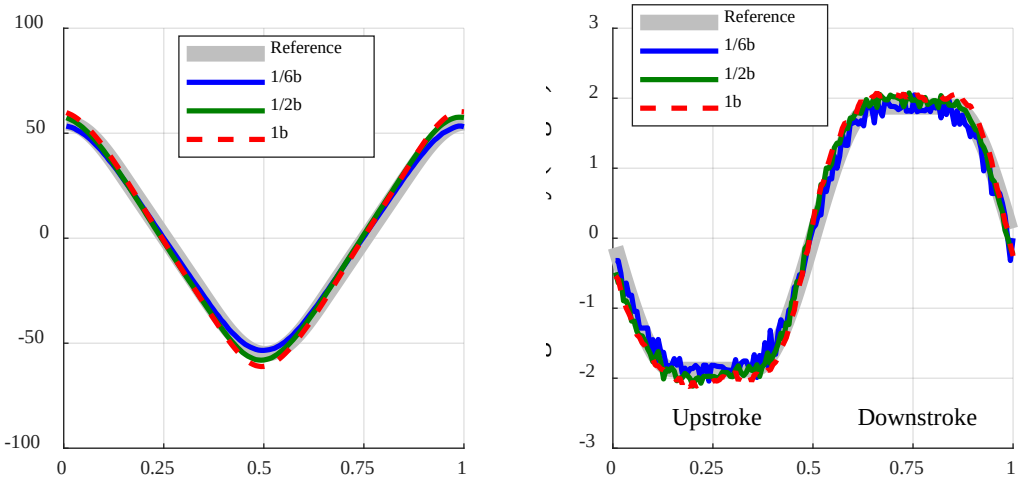

(a) Stroke amplitude (b) Angular velocity

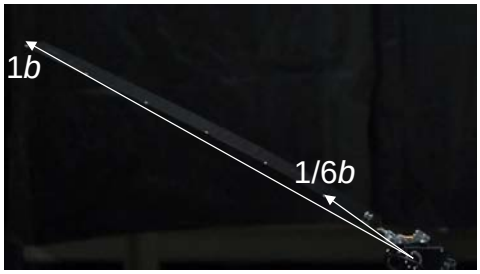

(c) Spanwise deformation at τ = 0.5 (end of upstroke)

Figure 5 – Spanwise deformation of the model flat plate in flapping motion

In order to evaluate the deformation of the model plates, we installed one commercial camera (A7III-R, Sony) behind the model at the end of the test section. A total of six markers on the AR = 3.0 plate were attached along a wingspan; these provided the time-historical locations at the spanwise cross-section. The camera collected 120 frames per second for ~10 seconds. A gradient-based pixel collector and an algorithm to find the maximum value (the peak in the image in Figure 4) were then used to determine the location of the markers at each frame; these algorithms are identical to that in the image pre-processing of modern PIV programs. The mask was also used for each marker, which was automatically generated in the code with the structural constraint and small tolerances, as shown in Fig. 3. The images have 1920 × 1080 pixels and the field of view was approximately 1,500 × 850 mm.

Figure 5 shows the angular positions of the six markers in a unit wingbeat cycle τ. A prescribed motion profile, which has a steady period of the constant stroke velocity and a fixed angle of attack during τ = 0.3 at each middle of the stroke, was an input to the robotic arm (gray thick lines). The wingbeat frequency and amplitude were 1 Hz and 110 deg (±55 deg). We found a slight deformation on the model flapping plate at each end of the stroke. The maximum difference was shown before reaching the end of the stroke, presumably due to higher inertia and non-optimal PID gain for the servo motor. During the stroke, on the other hand, we did not find any noticeable differences from the input profile. The angular velocities, which were obtained from the angular positions, (Fig. 4b) also showed steady values during the stroke, although those have a certain level of deviation (most of which was caused by the insufficient resolution of the raw images). This result indicates that the model flat plate driven by the robotic arm satisfies both the rigidity and lightweight with sufficient low inertia, and a rigid assumption would be adaptable for this study.

3. Results

3.1 Aerodynamic Characteristics of Stationary Plate

The force and moment measurement for the stationary cases (without motion) was done in advance. This was not only to extract the steady component from the sweeping plates, but to understand the LEV characteristics at a different Reynolds number from a previous study [11]. This was also a part of the study establishing a quasi-steady aerodynamic model. Because the advance ratio *J* was fixed in a current setup, the chord-based Reynolds number became the function of the aspect ratio, and it ranged from approximately 1.65 to 6.6 × 10^4. A span-based Reynolds number that is currently used at least for sweeping objects [12] was, however, fixed as ~10^5.

Figure 6 shows the C_L-α and C_D-α for the three AR plates of 1.5, 3.0, and 5.0. Every point was collected for 10 seconds with a sampling frequency of 1,000 Hz. Ensemble averaged trends in a few cases did not converge sufficiently, as we found unclear growth in the C_L in the pre-stall region. Fluttering near the stall angle that appeared during the test could also have amplified the maximum lift. Nevertheless, we saw a clear trend in the C_L with respect to the sweptback angle; an increase in the sweptback angle improved the maximum C_L. At AR = 1.5, the maximum C_L was found at β = 24 deg. This corresponds to approximately 20% of that at β = 0 deg. The increment in C_L is more dramatic at AR = 3.0. The maximum C_L at β = 36 deg marked 50% higher than that at β = 0 deg. The increment was also found at AR = 5.0, but the amount drastically decreased.

3.2 Aerodynamic Characteristics of Sweeping Plates

In contrast to water towing tank tests, which are a typical way of a flapping wing study (see [5] as an example), the wind tunnel tests requested a higher wingbeat frequency for a measurable change in dynamic pressure. This can result in substantial temporal delay and inappropriate profile transfer. In order to check this characteristic, we collected the real-time angular positions from each motor with the harmonic sampling frequency (four times lower than the sensor).

Figure 7 showed the result of the example case of AR = 5.0 during the three wingbeat cycles. The sweeping amplitude of the motion profile had 84 deg (± 42 deg), and the pitching axis was fixed as zero, i.e., no pitching motion. The wingtip velocity during the sweeping motion was approximately 2.5 m/s, which was identical to the freestream. *J* was 1.0, and the angle of attack, therefore, changed within ± 45 deg at the wingtip. This was also distributed from the wingroot to the wingtip from 0 to 45 deg as shown in Eq. (3) (refer to [8] in detail).

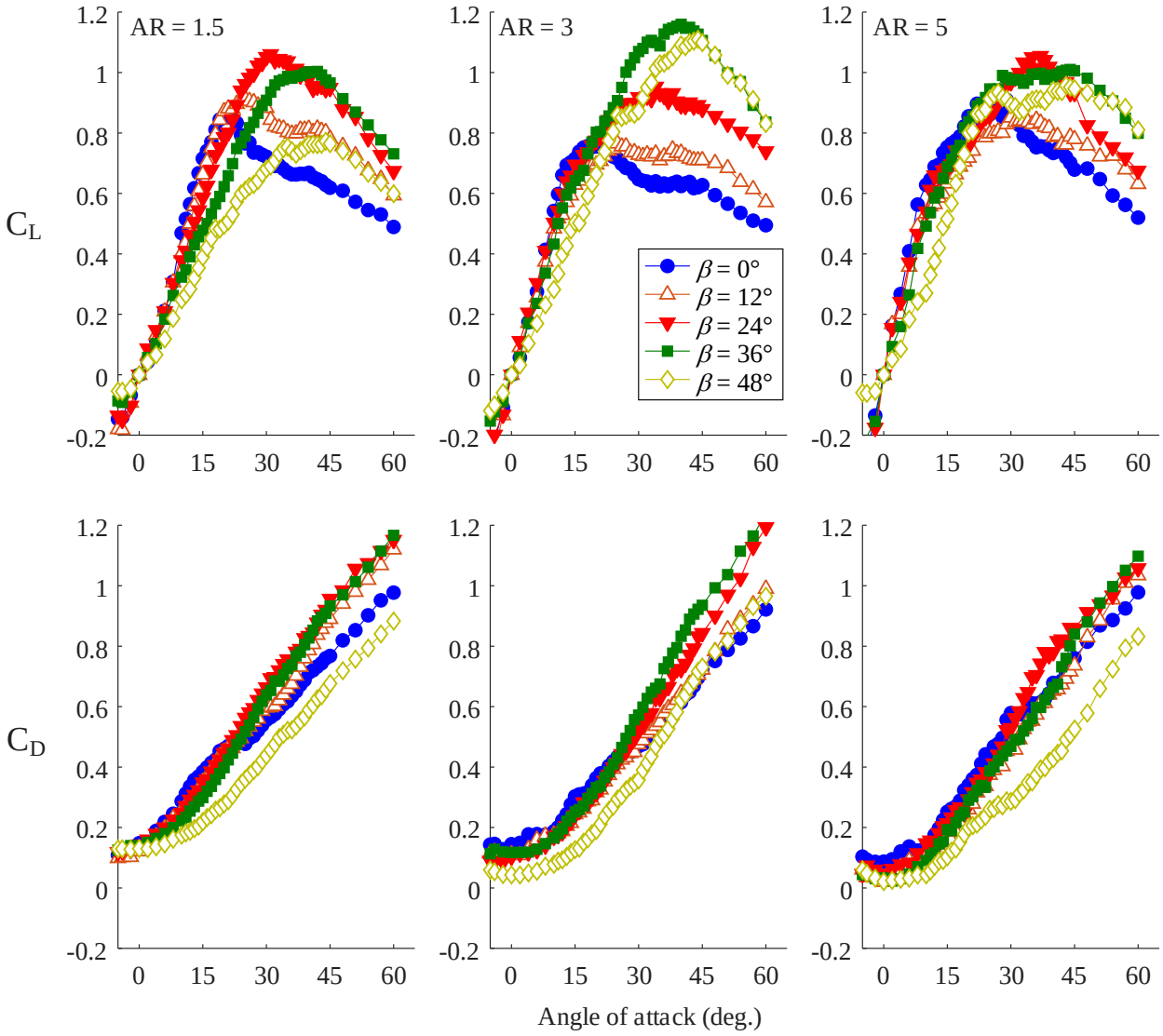

Figure 6 – C_L-α and C_D-α curves for the stationary cases

As shown in the topmost figure, the loads during the motion (inertia + aerodynamic force) eventually compromised the wingbeat motion and gave rise to a temporal gap between the input and output. The shape of the motion profile, however, was rarely affected in all cases. Based on the reference time points that were generated from the motion profile transmitter (green thin line), the temporal gap was obtained as 0.05 to 0.07τ.

Another crucial issue in the wind-tunnel test is how to get rid of an inertial and a gravitational force from a measured value. To this end, we employed two model plates that have different thicknesses for each case. Here, the identical planform of the model plates guarantees the identical aerodynamic force at the same wingbeat motion, and only the different mass and moment of inertia of the two plates create the different values in the measurement. The ratios of the masses and the moments of inertia are then the compensating coefficients to extract the aerodynamic force and moment. This method, however, would be only feasible when the same wingbeat motion is assured.

The last two graphs in Figure 7 show surface normal aerodynamic forces in the wing-fixed coordinate system ($^{W}F_{Z}$) at two different β of 0 and 30 deg. The 2-mm and 3-mm thickness plates were used to measure the force and moment, and the normal force was obtained after compensation (gray thick lines).

The reliability of the data here was relatively low; another treatment with a phase-locked averaging is highly necessary. However, we still were able to observe that the compensation effectively reduced the peak at the end of each stroke; this was almost not possible with the inertial forces calculated

with the inputted or measured wingbeat motion. The flattened force production at $\beta = 0$ deg and the increasingly produced force at $\beta = 30$ deg in the middle of stroke (light blue region) also have a good agreement with the previous study [8]. This also clarifies the potential of the approach using two plates having different thicknesses.

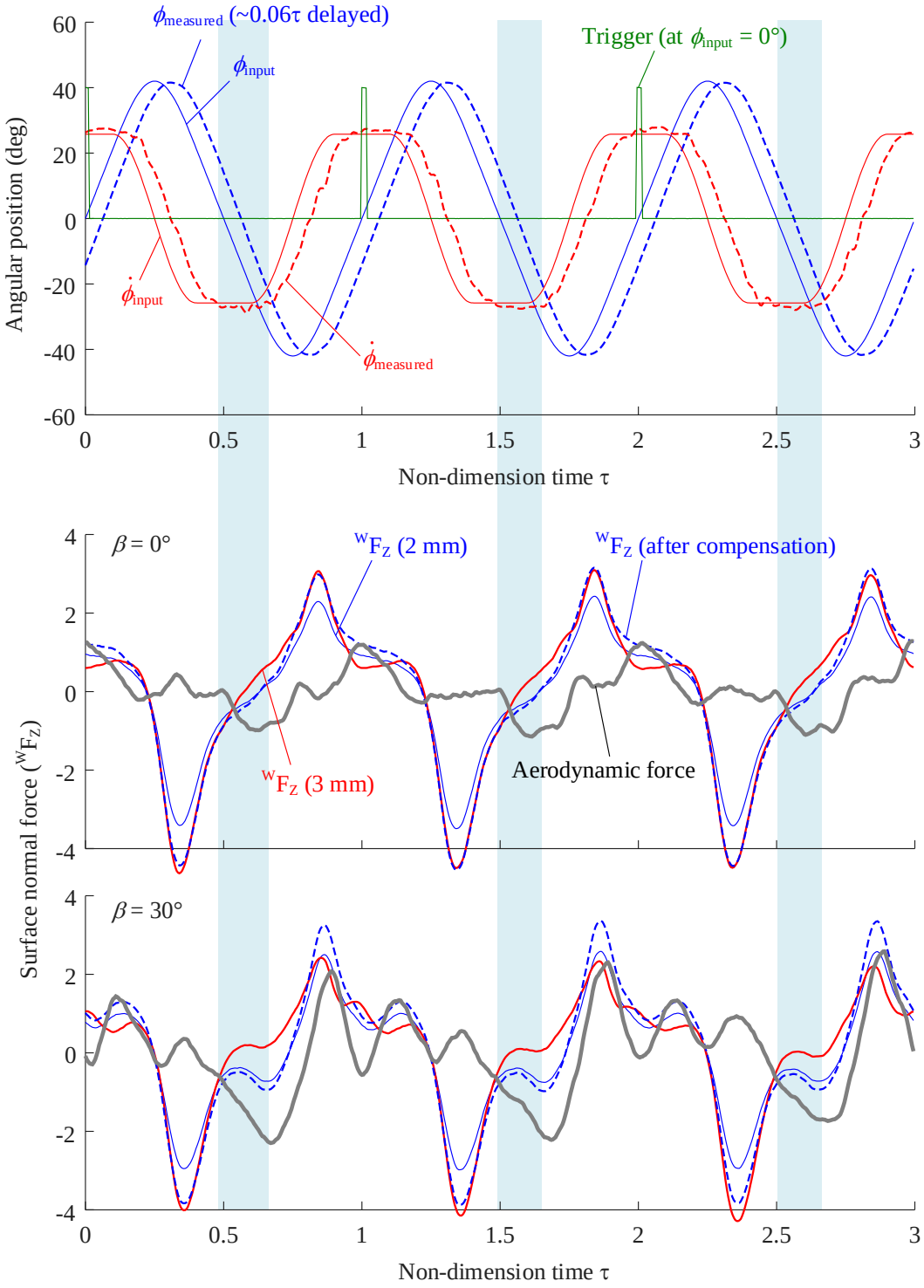

Figure 7 – Angular positions and the surface normal force on the sweeping AR = 5.0 plate.

4. Conclusion

In order to study the effect of freestream and wingbeat kinematics on the LEV, a wind-tunnel test was prepared. A servo-driven robotic arm was installed in a wind tunnel, and bending-beam loadcells were built to measure the small aerodynamic force and moment. Several model plates with different AR, which had been structurally optimized for the lightweight and low inertia, were also prepared.

The structural deformation of the model plates in sweeping motion has been investigated with a commercial camera and an in-house image processing code as a part of the study. The preliminary test for the effect of a sweptback angle showed a superior lift production with an increase in a sweptback angle regardless of the aspect ratio. As the previous study revealed, the aspect ratio of three had the highest value in the lift production with a sufficient sweptback angle. Tests for the sweeping plates were then conducted to investigate the effect of the wingbeat motion and advance ratio on the LEV. Here, two plates that had the same planform but two different thicknesses were used to eliminate the inertial force of the sweeping plates and to extract the aerodynamic force from the measured values. The result of the AR = 5.0 case showed a flattened lift production with no sweptback angle and an increasing lift production with time at the sweptback angle of 30 deg. This is in line with the previous study and clarifies the potential of the approach of how to eliminate the other force components from the measured values.

5. Contact Author Email Address

js.han@tum.de

6. Copyright Statement

Acknowledgments

The project is funded by the Deutsche Forschungsgemeinschaft (DFG, German Research Foundation) – grant number HA 9127/2-1.

References

[1] Breitsamter, C. (2008). Unsteady flow phenomena associated with leading-edge vortices. *Progress in Aerospace Sciences*, *44*(1), 48-65.

[2] Chin, D. D., and Lentink, D. (2016). Flapping wing aerodynamics: from insects to vertebrates. *Journal of Experimental Biology*, *219*(7), 920-932.

[3] Lentink, D., & Dickinson, M. H. (2009). Biofluiddynamic scaling of flapping, spinning and translating fins and wings. *Journal of Experimental Biology*, *212*(16), 2691-2704.

[4] Lentink, D., & Dickinson, M. H. (2009). Rotational accelerations stabilize leading edge vortices on revolving fly wings. *Journal of experimental biology*, *212*(16), 2705-2719.

[5] Han, J. S., Chang, J. W., & Cho, H. K. (2015). Vortices behavior depending on the aspect ratio of an insect-like flapping wing in hover. *Experiments in Fluids*, *56*(9), 1-16.

[6] Kruyt, J. W., Van Heijst, G. F., Altshuler, D. L., & Lentink, D. (2015). Power reduction and the radial limit of stall delay in revolving wings of different aspect ratio. *Journal of the Royal Society Interface*, *12*(105), 20150051.

[7] Jardin, T., & Colonius, T. (2018). On the lift-optimal aspect ratio of a revolving wing at low Reynolds number. *Journal of The Royal Society Interface*, *15*(143), 20170933.

[8] Han, J. S., & Breitsamter, C. (2021). Aerodynamic investigation on shifted-back vertical stroke plane of flapping wing in forward flight. *Bioinspiration & biomimetics*, *16*(6), 064001.

[9] Han, J. S., Chang, J. W., & Han, J. H. (2016). The advance ratio effect on the lift augmentations of an insect-like flapping wing in forward flight. *Journal of Fluid Mechanics*, *808*, 485-510.

[10] https://www.epc.ed.tum.de/aer/windkanaele/windkanal-b/

[11] Han, J. S., & Breitsamter, C. (2021). Leading-Edge Vortex Characteristics of Low-Aspect-Ratio Sweptback Plates at Low Reynolds Number. *Applied Sciences*, 11(6), 2450.

[12] Harbig, R. R., Sheridan, J., & Thompson, M. C. (2013). Reynolds number and aspect ratio effects on the leading-edge vortex for rotating insect wing planforms. *Journal of Fluid Mechanics*, 717, 166-192.